Chapter 9

Detectors

For a chosen wavelength of light, the material demands for waveguides and detector/light sources are contradicting with respect to matter-light interaction. For the waveguide one wants absorption as low as possible, and for the detector it should be high. That means the material for detectors has to be different from that of the waveguides, leading to two prevalent system concepts for Si photonics:

- High-bandgap (insulator) waveguide with a Si detector
- Si waveguide with a low-bandgap detector

In this chapter, we discuss detector principles, system and wavelength considerations, detector structures, and high-speed operation and give selected experimental results.

9.1 Detection Principles

In principle, each matter-light interaction could be used to sense impinging light. In practice three main principles (Table 9.1) dominate: photon detectors, thermal detectors, and coherent detection (heterodyne detection).

Silicon-Based Photonics
Erich Kasper and Jinzhong Yu

ISBN 978-981-4303-24-8 (Hardcover), 978-1-315-15651-4 (eBook)
www.jennystanford.com

Table 9.1 Detection principles used in photodetectors

Photon detectors	Thermal detectors	Coherent detection (amplitude/phase)
Chemical change > photoplates Photoconductors (intrinsic/extrinsic) Photodiodes/phototransistors Photoemissive detectors (photomultipliers, microchannel plates)	Bolometers	Mixing with a coherent local oscillator/laser

The broadest group—photon detectors—uses the large variety of effects when light meets atoms or solids. They create chemical changes in photoresists or photoplates (the original effect in photography), modulate the conductivity in photoconductors, or generate photocurrents in photodiodes/phototransistors and solar cells, or a different frequency is generated by mixing with a local oscillator/laser in coherent detection (a method that is the common technical choice in high-performance electrical detection—but difficulties with laser integration and phased lock-loop frequency stabilization prevented their rapid introduction to optoelectronic detection). The heating caused by the absorbed energy is used in bolometers for mid- and far-infrared (MIR and FIR) detectors where the low photon energy requires cooling of small-bandgap semiconductors in photon detectors. In a semiconductor system otherwise photocurrent generation in photodiodes/phototransistors is the preferred method for light detection. In phototransistors the detecting part is also a diode function; the transistor structure may be used for first-stage amplification.

The discussion for a certain detector is mainly made with respect to the photodetector parameters given in Table 9.2.

Table 9.2 Important parameters for photodetectors

Quantum efficiency	Spectral response
Noise bandwidth	Time response/frequency
Linearity	Size and numbers of pixels
Dynamic range	Operation temperature

For integrated systems the spectral response, the quantum efficiency, and the frequency bandwidth are the most important parameters.

9.2 Detector Configuration and Wavelength Considerations

Of primary importance for the detector configuration is the angle of incidence of light.

9.2.1 Vertical Incidence Detection

For image sensors a vertical incidence is the standard situation. Figure 9.1 shows the scheme of a future detector array embedded in a system on chip (SOC) consisting of the detector array, a logic part in complementary metal-oxide silicon (CMOS) technology, and high-frequency (radio frequency [RF]) input/output connections. Heterobipolar transistors (HBTs) for millimeter-wave operation speed (30–300 GHz) drive the RF components.

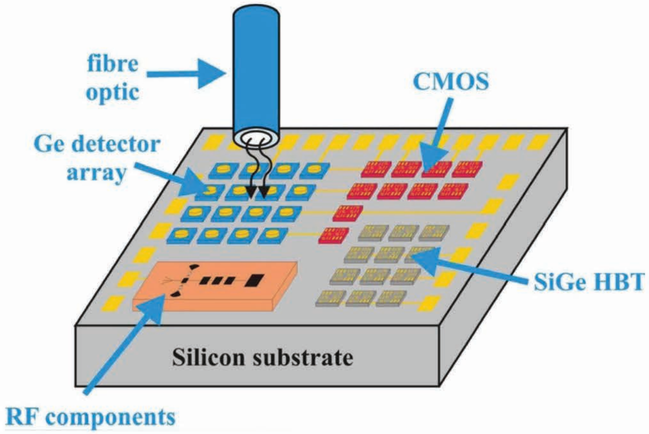

Figure 9.1 Integrated Ge detector array in a system on chip (SOC) comprising the detector array, a high frequency (RF) part with SiGe HBTs, and a CMOS logic. Reprinted by permission from Springer Nature Customer Service Centre GmbH: Springer Nature, *Frontiers of Optoelectronics in China*, Ref. [1], copyright (2010).

In this figure, the array is made from Ge detectors for near-infrared (NIR) vision as requested in automotive assistance systems for pedestrian detection. Vertical incidence allows efficient and fast detection if the absorption is strong at the selected wavelength. In detector arrays, a read-out circuitry is added to the sensor. The scheme is shown (Fig. 9.2) in the example of the CMOS image sensors, which are now in broad use in consumer electronics.

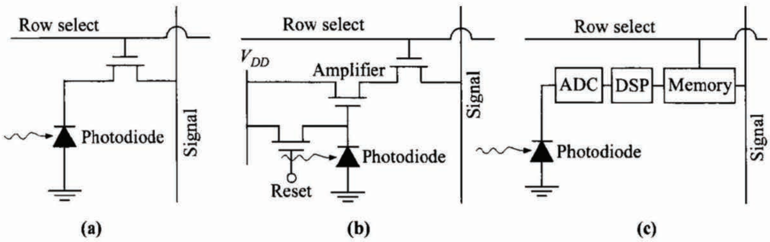

Figure 9.2 Different versions of CMOS image sensors: (a) passive pixel sensor (PPS); (b) active pixel sensor (APS); and (c) digital pixel sensor (DPS).

The simple form is the passive pixel sensor (Fig. 9.2a), where the photodiode is connected with a metal-oxide-silicon (MOS) transistor whose gate is terminated at the row line whereas the signal line is in contact with the transistor output (drain). With a proper gate voltage on the row select line all transistors of this line are on and the signals of the photodiodes on this row line can be read out with the signal lines. Active pixel sensors have already included an amplifier to read out the amplified signal (Fig. 9.2b). Digital pixel sensors give their analog signal to an analog-digital converter, where it is converted to a digital signal, processed in a digital signal processor, and saved in a memory.

9.2.2 Lateral Incidence Detection

A lateral incidence is more convenient for on-chip waveguide systems and for coupling to fiber optics. Even for original vertical incidence on the chip, a coupling structure to lateral incidence on the photodiode is applied if relaxed adjustment and high-speed operation are in demand. We will discuss this topic in more detail in the speed section. A scheme of lateral incidence of light via a planar waveguide (right side) is shown in Fig. 9.3, where the high-frequency electrical contacts (left side) are already given as **copl**anar electrical **w**aveguide (CPW) in a ground (G)–signal (S)–ground (G) configuration. CPWs from thin metal lines allow electrical signal transfer at high speeds of up to more than 100 GHz.

(Remark: Do not confuse the abbreviations G and S used for ground and signal contacts with the same abbreviations used for gate and source contacts in transistor technology).

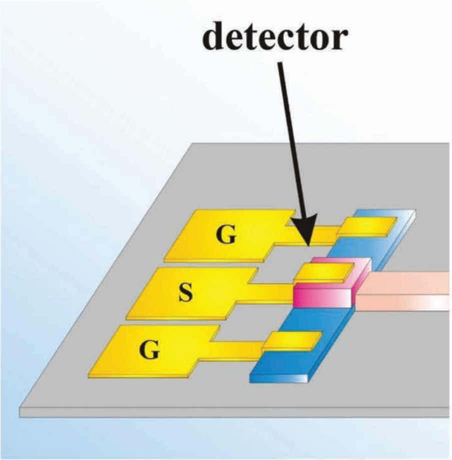

Figure 9.3 Scheme of a lateral waveguide Ge detector (arrow) with light coupled in from a Si waveguide. The Si waveguide (coming from the right side) is butt-coupled to the Ge detector. The high-speed electrical signal readout (on the left side) is realized by a coplanar electrical waveguide (CPW) with symmetric ground contacts (G) to the bottom layer and the central signal line (S) to the top layer of the Ge-on-Si p-i-n detector structure.

9.2.3 Wavelength Selection

Either the selected wavelength is defined by the needs of an intended application, or it is selected by a tradeoff between properties of available materials, technologies, and devices. Some applications need specific wavelengths; for example, processing of telecommunication signals is concentrated on bands around 1.3 μm and 1.55 μm. Sensors for environmental gas detection, for example, for methane or carbon dioxide, rely on larger wavelengths in the MIR regime because there are specific absorption bands for molecules.

The wavelengths of on-chip data transfer may be chosen to fulfill high bandwidths and convenient technological device fabrication. Si waveguides are transparent for wavelengths above 1.2 μm. Foundry service for Ge on Si devices is available that opens the wavelength window up to 1.6 µm for slightly tensile strained Ge. Devices with cutoff wavelengths above 1.6 µm are available in cooperation with research institutions focusing on highly tensile strained Ge, metastable GeSiSn alloys, or III/V epitaxy on Si.

For the detector material, a rather small absorption depth d_α is requested to minimize device size and to improve device speed.

$$d_\alpha = 1/\alpha \tag{9.1}$$

Practical values of α are typically in the range of 10^3/cm to 10^5/cm, which corresponds to absorption depths from 10 µm to 0.1 µm. Exceptions from this rule are allowed in silicon, where the high quality of material delivers diffusion lengths of up to millimeters, facilitating minority carrier transport from even the substrate backside to the frontside junction. This can be exploited in solar cells or slow photodetectors where an absorption range from $\alpha = 10^{-1}$/cm can be utilized.

In the following, we consider the absorption properties of some specific semiconductors (for a general discussion of absorption see Chapter 3), with emphasis on the SiGe material system.

In Fig. 9.4, the absorption coefficient α is given for several common semiconductors: GaAs, Si, Ge, and GaInAs. The III/V

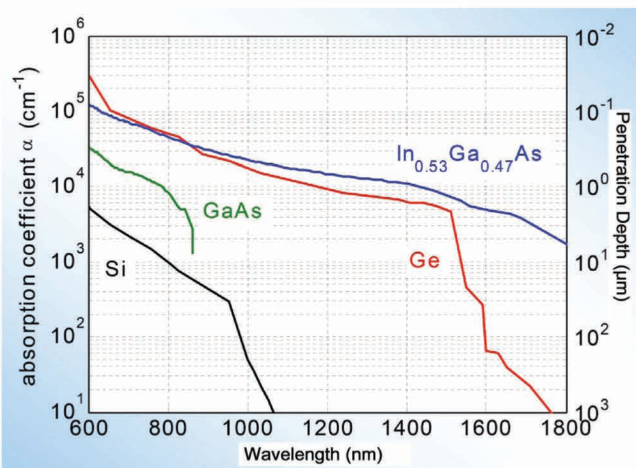

Figure 9.4 Absorption in common semiconductors (Si, GaAs, InGaAs, and Ge are selected). Given is the absorption coefficient as a function of wavelength.

semiconductors GaAs and GaInAs are direct semiconductors with different bandgaps. Above the bandgap energy $E_{gdir,}$ photons are easily absorbed—in the often-chosen presentation as a function of wavelength (like in Fig. 9.4) this means strong absorption below the corresponding wavelength λ_g, where

$$\lambda_g\,(\mu m) = 1.24\ \mu m/E_g\,(eV). \tag{9.2}$$

Both silicon and germanium are indirect semiconductors [2] where absorption below the wavelength λ_g increases much slower, as shown in the Si case. Fundamental absorption [3] starts below λ_g = 1.1 μm but increases only up to $5 \cdot 10^3$/cm at λ = 0.6 μm, nearly an order of magnitude below GaAs, for which absorption starts at λ_g = 0.93 μm, steeply crossing the Si absorption curve at about λ = 0.85 μm. However, hybrid absorption curve characteristics are seen if one looks at Ge. At the bandgap wavelength (λ = 1.85 μm) the absorption curve starts slowly, like in Si, but suddenly at about λ = 1.6 μm, the curve steepens and reaches that of the direct semiconductor InGaAs. The explanation for these absorption characteristics of Ge is given by its conduction band details [4]. For the explanation, let us start with the more familiar conduction band of Si (Fig. 9.5).

The bandgap is defined by the electron energy difference between the conduction band minimum and the valence band maximum. The valence band maximum is always at the wave vector length k = 0 (named the Γ point), whereas the electron energy minimum of the conduction band is at a finite k value in the case of an indirect semiconductor. In the case of Si, the minimum conduction band energy is at the Δ (delta) point of the Brillouin zone, which is in the x direction (in Si 0.8X). In the cubic diamond lattice, the y and z directions and their minus signs are equal to the x direction, which means that the energy minimum is sixfold degenerate, as best seen in a constant energy surface (see Fig. 9.5, top) presentation. The lowest direct transition is far above this indirect bandgap energy, at about E_{gdir} = 3.4e V, which corresponds to an ultraviolet (UV) photon (λ = 364 nm). In Si, the absorption in the NIR and the visible (VIS) spectrum is solely dominated by the indirect absorption. In Ge the lowest direct transition comes strongly down to E_{gdir} = 0.80 eV whereas the X transition is only slightly reduced compared to Si (E_{gX} = 0.85 eV). In spite of this crossing of Γ and X transition the semiconductor Ge is an indirect one because the L transitions (111 direction, cube diagonal) decrease more than the X transitions to E_{gL} = 0.66 eV (all values given for room temperature). The degeneracy of the L minimum in the conduction band is fourfold; see the constant energy surface in Fig. 9.5 (eight energy ellipsoids are drawn, but energy ellipsoids at the zone edge between first and second Brillouin zones count only half for the measure of degeneracy). This indirect bandgap causes the weak absorption start at $\lambda = 1.85$ μm whereas the only slightly higher direct transition ($\lambda = 1.55$ μm) is responsible for the steep absorption increase around that direct transition. Heating the device (self-heating or forced heating) reduces the bandgap of diamond-type semiconductors and extends by that way the infrared range.

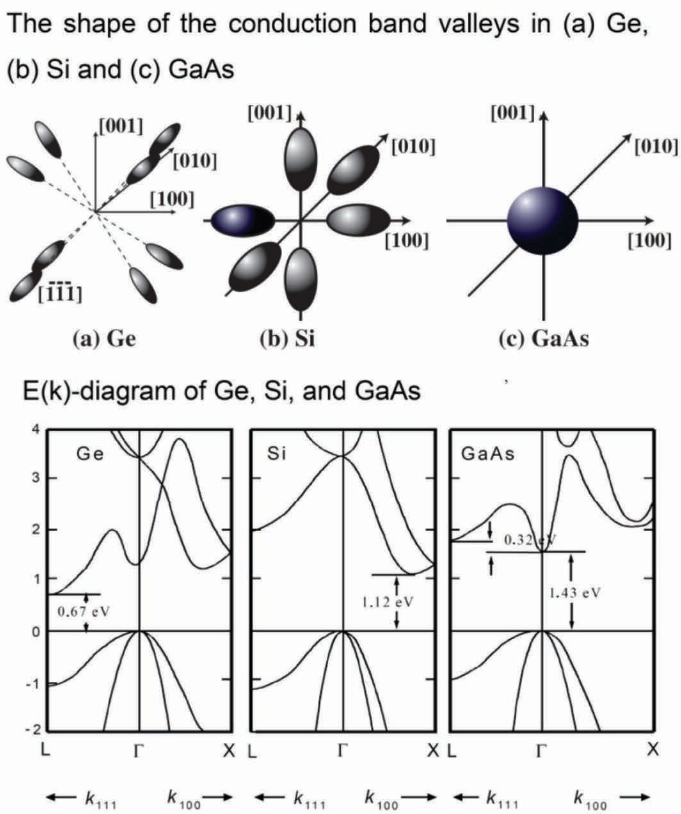

Figure 9.5 Constant energy surfaces for conduction band electrons (top part of the figure). Band structure (energy *E* versus wave vector length *k*) of common semiconductors Si, GaAs, and Ge (lower part of the figure). Given are the energies of carriers as a function of the wave vector *k* (center Γ, $k = 0$, X point in 100 direction, L point in 111 direction), using data from Refs. [1, 3, 4].

The transition from Si to Ge can easily be observed with SiGe alloys with increasing Ge amounts (Fig. 9.6).

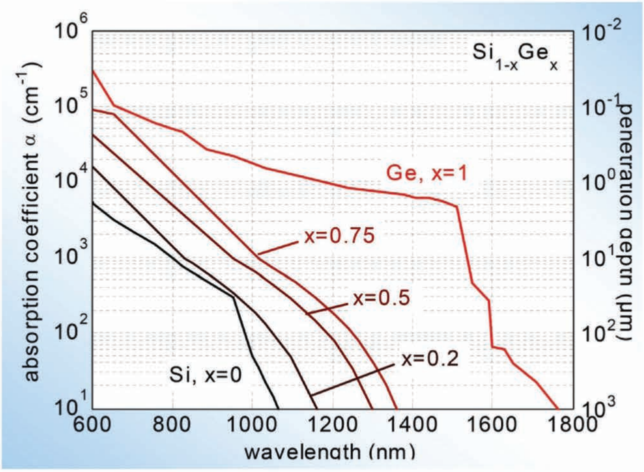

Figure 9.6 Absorption versus wavelength of SiGe alloys with different Ge amounts x, from pure Si ($x = 0$) to pure Ge ($x = 1$).

In Fig. 9.6, SiGe alloys with Ge amounts $x = 0, 0.2, 0.5, 0.75$, and 1 are selected. With an increasing Ge content the absorption curve is shifted to the infrared corresponding to the lowering of the indirect bandgap energy. The bandgap lowering ΔE_{gx} of SiGe (compared to Si) is nonlinear, given in parabolic description [2] as

$$\Delta E_{gx} = -0.43x + 0.206x^2 \text{ (in eV) for } x \leq 0.85. \tag{9.3}$$

The Δ valley is the lowest one up to a Ge amount $x = 0.85$. All SiGe alloys up to very high Ge amounts (85%) have a Si-like conduction band minimum (Δ point). Only above $x \geq 0.85$ the L minimum comes down below the Δ minimum. The L minimum in the Ge-rich range ($x > 0.85$) is described by a linear dependence on x. We compare now the indirect L minimum energy of SiGe with that of Ge:

$$\Delta E_{gL} \text{ (compared to Ge)} = 1.27(1 - x) \qquad \text{(in eV)} \tag{9.4}$$

An extrapolation of this linear behavior yields an L minimum of 2.01 eV for Si, which is within the reasonable range of what is shown in Fig. 9.5.

The bandgaps deduced from photoluminescence (PL) and absorption differ by up to 40 meV. A part of the difference may be explained by the finite exciton (electron-hole pair) binding energy E_b, which varies from 14.5 meV for Si excitons to 4.1 meV for Ge excitons. From PL measurements, the exciton bandgap ($E_g - E_b$) will be measured at low temperatures. With increasing temperature, the bandgap E_g shrinks, for example, for Si from 1.17 eV at 0 K to 1.118 eV at 300 K or for SiGe ($x = 0.78$) from 0.915 eV to 0.87 eV. This means the Δ minimum (remember this minimum dominates up to $x = 0.85$) shrinks at about 5% for 300 K independent of the Ge content. The temperature dependence of the L minimum is definitely stronger, at about 11% for 300 K in Ge (0.74 eV at 0 K; 0.66 eV at 300 K).

Within the discrepancy of 40 meV between emission and absorption experiments, the bandgap of unstrained SiGe is well described. What is the situation with the direct transitions for the whole range of SiGe compositions? The critical points of the density of states (named E_0, E_1, and E_2) are mainly investigated by spectroscopic ellipsometry, reflectometry, and modulation spectroscopy (electroreflectance and thermoreflectance). The most important signatures in refractive index and absorption stem from the E_1 and E_2 transitions. The E_1 transition marks the highest n value, whereas the absorption peak is near the E_2 transition [3]. The E_1 transition shifts with the Ge amount x as follows:

$$E_1(x) = 3.395 - 1.44x + 0.153x^2 \text{ (in eV)} \tag{9.5}$$

From ellipsometry or reflectometry the Ge content may be deduced from the E_1 position

$$x = 4.707 - (6.538E_1 - 0.0397)^{0.5}. \tag{9.6}$$

The spin-orbit split energy gap $E_1 + \Delta_1$ is slightly larger:

$$E_1 + \Delta_1 = 3.428 - 1.294x + 0.062x^2 \text{ (eV)} \tag{9.7}$$

The split Δ_1 increases from 33 meV at Si to 88 meV at the Ge side. The E_2 transition (near the X point) is nearly independent of the Ge amount, $E_2 = 4.4$ eV. The direct transitions at the Γ point ($k = 0$) are E_0, $E_0 + \Delta_0$, and E_0'. The gap E_0' decreases very slightly with Ge amount

$$E_0' = 3.40 - 0.3x \qquad \text{(in eV)}. \tag{9.8}$$

The transition, which dramatically changes with Ge amount, is the E_0 transition.

This transition comes down from 4.05 eV in Si to 0.8 eV in Ge, and it is the lowest direct transition up from about $x = 0.35$ (on the Si side the E_0' and E_1 transitions are the lowest direct ones).

Linear interpolation gives

$$E_0 = 4.05 - 3.25x \text{ (in eV)}. \tag{9.9}$$

The spin-orbit split energy Δ_0 increases with the Ge amount from 44 meV to 290 meV.

The strong dependence of E_0 transition on the Ge amount causes Ge to be a pseudo-direct absorber because only a further shift of 140 meV would be necessary to cross the direct Γ and indirect L transitions. In emission, the indirect character dominates in relaxed Ge, but we will discuss in the following chapters strategies with strain, alloying, and doping to also strengthen direct emission processes.

In Fig. 9.7 we summarize the results for unstrained SiGe alloys.

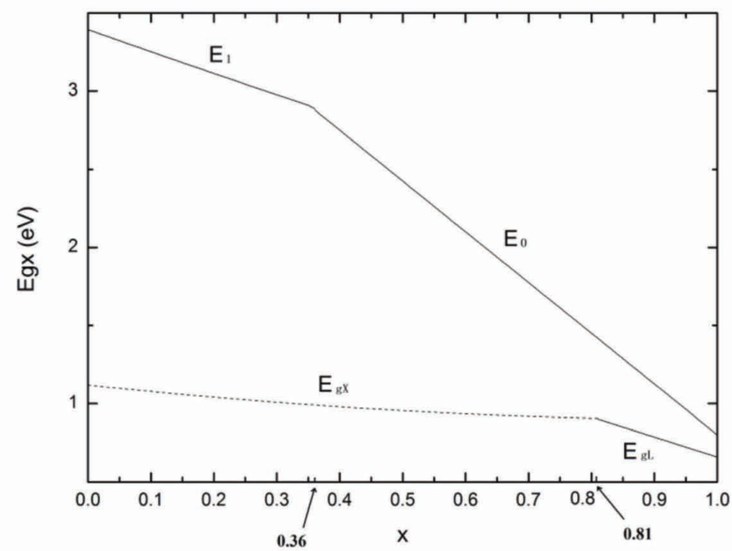

Figure 9.7 Direct and indirect band transitions in SiGe alloys. Shown are only the lowest direct transitions (E_1 at a low Ge amount and E_0 at a higher amount) and the lowest indirect transitions E_{gX} and E_{gL}.

The solid line shows the lowest direct transition (E_1 in SiGe, $x \leq 0.35$; E_0 in SiGe with $x > 0.35$) compared with the dotted line for the lowest indirect transition (X transition, $x < 0.85$; L transition, $x \geq 0.85$). On the Si side the direct transitions E_0' and E_1 need about

3 eV (UV light necessary) whereas the indirect transition X needs only more than 1.1 eV. Above x = 0.35 the strongly decreasing E_0 gap defines the lowest direct transition whereas above x = 0.85 the indirect L gap replaces the X gap.

We have already discussed the temperature dependence of indirect transitions. The temperature coefficients of the direct transitions are found to be on the order of –0.2 meV/K to –0.5 meV/K. The main reason for the negative temperature effects is given by the lattice expansion, which is accompanied by shrinking gaps.

The majority of data of unstrained alloys are collected from bulk samples. In heterostructure layers both compressive and tensile strain are usually found as a result of lattice mismatch (SiGe on Si is compressively strained) and thermal expansion mismatch (unstrained Ge/Si cooled down from epitaxy temperatures to room temperature exhibits tensile strain). For heterostructure devices the strain status has to be defined and the strain effects have to be described and explained.

9.3 Photon Detector Structure

A photoconductive device realizes the simplest photodetector. It exploits the change in conductivity of a semiconductor that is illuminated. The intrinsic photoconductivity involves the excitation of electrons and holes from a photon absorption process. This process occurs when the energy of the photon exceeds the bandgap energy. The technological realization needs ohmic contacts on both sides of the illuminated area. A voltage bias is applied on these contacts. The current through the device increases under illumination because of the additional carriers caused by absorption. This detector principle functions not only for a single crystalline material but also for polycrystalline or amorphous materials. Therefore, it is frequently used in early phases of material testing when technology is under development.

Photodiode detectors dominate in the VIS and NIR spectrum range because of good properties in detectivity and speed. In the following sections, we will discuss different technological realizations of photodiode detectors.

9.3.1 P/N Junction Photodiode

The basic detector structure [4] is shown in the example of a p-i-n diode (Fig. 9.8).

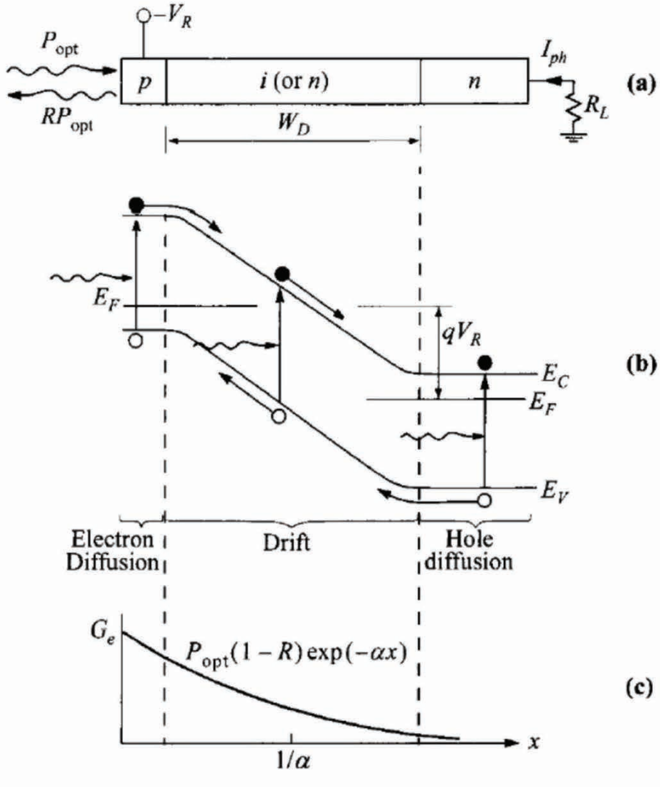

Figure 9.8 Operation of a p/n junction photodiode: (a) Cross-sectional view of the p-i-n diode. (b) Energy band diagram under a reverse bias. (c) Carrier generation characteristics (using data from Refs. [1, 4]).

A nominal intrinsic semiconductor (i-layer) absorption layer (Fig. 9.8a) is terminated on both sides by highly doped layers of the opposite carrier type. In Fig. 9.8a, light of power P_{opt} is entering from the left. A part $R \cdot P_{opt}$ is reflected (R is reflectivity) so that the power $P_{opt} \cdot (1 - R)$ penetrates into the semiconductor. On a bare semiconductor the reflectivity R is high because of the high refractive index n of semiconductor materials.

$$R = \left(\frac{n-1}{n+1} \right)^2 \tag{9.10}$$

In the very high absorption spectral range, the complex n value has to be taken, which then reads

$$R = 1 - 4n / (n^2 + \kappa^2 + 2n + 1). \tag{9.11}$$

The relative change in reflectivity

$$\frac{dR}{dk} = \frac{(1-R)^2}{2n} \cdot \kappa \tag{9.12}$$

is proportional to the absorption index κ but with a low prefactor of about 0.05 for a semiconductor with a refractive index n = 4. A considerable shift in R (>10%) by the influence of the very high absorption index κ is given roughly by a κ value of more than 1. Looking at a table of optical constants [3], one finds for Si, SiGe, and Ge an upper photon energy below which absorption is nearly negligible for the calculation of reflectivity.

These energy levels are 3.25, 3.1, 3, 2.85, 2.6, 2.3, and 2 eV for the above given SiGe alloy row with x = 0, 0.1, 0.2, 0.3, 0.5, 0.75, and 1, respectively.

The high reflectivity of semiconductors makes antireflection coatings of photodiodes a must for exploitation of the full responsivity potential. We will discuss technical details in the next section.

The electric field $\vec{F}$ in an ideal intrinsic (i) layer is easily calculated by

$$\vec{F}_\mathrm{i} = \text{const.} = (V_\mathrm{bi} - V) / d_\mathrm{i}, \tag{9.13}$$

with V_bi, V, and d_i as built-in voltage, applied voltage (negative value for reverse diode voltage!), and thickness of the intrinsic layer, respectively. The field is only slightly penetrating in the surrounding highly doped layers. Let us assume for this first approach that the doping in the n and p layers is high enough for one to be able to neglect this field penetration. The energy band diagram is then as shown for a reverse bias in Fig. 9.8b. The energy is linearly varying if the field is constant. Figure 9.8c shows the spatial distribution of the carrier generation rate $G_\mathrm{e} = G_\mathrm{p} = G$ inside the semiconductor when for simplicity no backside reflection is considered.

$$G = (1-R)\exp(-\alpha x) \cdot P_\mathrm{opt} / A \cdot (\hbar\omega) \tag{9.14}$$

Here R is reflectivity, α is the absorption coefficient, P_{opt}/A is the power density (A is area), and $\hbar\omega$ is photon energy.

A note on the term intrinsic is necessary before we discuss the electrical field $\vec{F}$ and the band diagram. Physically correct, the term "intrinsic" would require that the doping be below the intrinsic carrier concentration. In silicon the room temperature intrinsic carrier concentration is about 10^{10} cm^{-3}, which is orders of magnitude below the technical possibilities of 10^{13} cm^{-3} – 10^{16} cm^{-3} background doping N_b in bulk or epitaxial layers. In a technical sense, the term "intrinsic" is less strictly used when the i-layer is fully depleted at zero bias (at the built-in voltage V_{bi}). The i-layer is termed ν-layer (n-background) or π-layer (p-background), respectively, if the type of background doping is known. The electric field decreases linearly from a maximum at the junction (n^+/p or p^+/n for p- or n-background, respectively). The slope of the field strength decrease depends on the background doping.

A one-sided abrupt p/n junction follows immediately from the p-i-n if the intrinsic layer is higher doped (e.g., in the 10^{17} cm^{-3} range compared to the 10^{20} cm^{-3} range for the electrode layers). Then the depletion layer ends within the now-doped absorption layer.

The following summarizes some textbook formulas for the basic properties of the depletion layer in a one-sided p/n junction (p-doping high and n-doping moderate with density N_D).

The built-in voltage

$$V_{\mathrm{bi}} = (k_B T / q)\ln(N_D \cdot N_A / n_i^2). \tag{9.15}$$

Here N_A is doping of the p electrode and n_i is intrinsic carrier density.

The depletion width

$$d_{\mathrm{depl}}^2 = (2\varepsilon_S / q)(1 / N_D)(V_{\mathrm{bi}} - V). \tag{9.16}$$

Here ε_s is the dielectric constant of the semiconductor and V the applied voltage (positive sign in forward direction). The maximum field strength E_m (at the interface) is as follows:

$$E_m^2 = (2q / \varepsilon_S) \cdot N_D \cdot (V_{\mathrm{bi}} - V) \tag{9.17}$$

or

$$E_m = \left(\frac{q}{\varepsilon_S}\right) N_D \cdot d_{\mathrm{depl}} \tag{9.18}$$

(if d_{depl} is known).

These textbook formulas use the so-called Schottky approximation, which assumes charge contributions only from the dopant atoms in the depletion region.

Approximations that are more refined take care of the diffusion tails of the depletion edge and of bandgap shrinkage in highly doped layers. The diffusion tails lead to a slight modification of Eq. 9.15 in that V_{bi} is replaced by $(V_{bi} - 2k_BT/q)$; the high doping causes a bandgap shrinkage, which is described in electronic devices by an increase in the intrinsic carrier concentration. Furthermore, the full Fermi–Dirac statistics have to be used instead of the Boltzmann approximation. For details, the interested reader should refer to books on semiconductor device physics [5].

The generation rate G decreases, like light intensity, exponentially with the absorption penetration depth as decay length. We now have to determine whether a carrier pair is generated in the depletion region (i-region) or in the surrounding region. A pair generated in the depletion region is separated by the high electric field, and the carriers are collected by the p and n electrodes if the quality of the material is not too bad. The pairs generated in the surrounding regions move randomly because of the lack of an electric field. The minority carriers may diffuse to the junction and contribute to the photocurrent. The diffusion is strong within the diffusion lengths L_n and L_p for electrons (in p material) and holes (in n materials), respectively. The diffusion length L is connected to two fundamental properties of a semiconductor, the minority carrier diffusion coefficient D and the recombination lifetime τ. For electrons the relation reads (for holes the index is p)

$$L_n^2 = D_n \cdot \tau_n . \tag{9.19}$$

This is a general law for Brownian motion linking the square of the length with the product of the diffusion constant times the time. The diffusion constants are linked to the mobility μ via

$$D_n = \mu_n (k_B T / q). \tag{9.20}$$

Here the thermal voltage k_BT/q is the proportionality constant (k_B is Boltzmann constant, T is temperature, and q is the electron charge).

The diffusion length L is rather large in low-doped semiconductors, and there it is used as a quality criterion because the recombination lifetime τ in indirect semiconductors is given by the recombination across midgap energy levels of metallic or defect traps. In high-doped semiconductors the lifetime is strongly reduced by Auger recombination (transfer of the momentum to a nearby carrier instead of phonon generation), resulting in submicrometer diffusion lengths in the p and n electrodes. Diffusion increases the internal quantum efficiency in solar cells, for which quantum efficiency is more important than speed (a field-free motion like diffusion is much slower compared to the fast velocity of electrons/holes in the strong electric field of the depletion layer). In high-speed applications, the diffusion current is minimized despite design constraints to get high quantum efficiencies. The design constraints of microwave and millimeter-wave-frequency-modulated detectors are treated in a separate section later. Here, only an order of magnitude assessment of the time constants in diffusion is given. Assume L = 100 nm and D = 1 cm^2/s; then the time constant will be 0.1 ns, which is acceptable up to a modulation frequency of 1 GHz.

The given relations are valid not only for Si but also for other semiconductors. The numerical values of the depletion layer properties differ because of different values of the intrinsic carrier density n_i. In heterojunctions, the band discontinuities disrupt the smooth energy function known from homojunctions. The band discontinuities of the valence and conduction bands are a typical electronic property of a pair of semiconductors. They depend on the chemical composition and the strain status of the heterostructure couple.

The key mechanism of all photocurrent-based detectors is the separation of carriers by the electric field of a depletion layer. In different types of detectors this depletion layer may be created instead of a p-i-n or p/n junction, by metal-semiconductor junctions (Schottky contact) or metal-insulator-semiconductor (MIS) junctions (MIS or MOS diode).

9.3.2 Schottky Photodiode

In a metal-semiconductor junction (Schottky contact), the depletion layer is caused by the charge transfer due to the work function differences of metal and semiconductor. For the depletion layer formula only a lower built-in voltage appears, replacing Eq. 9.15 by Eq. 9.21.

$$V_{bi} = (\text{Schottky} - \text{contact}) = \Phi_B - \Phi_{nF} \tag{9.21}$$

Φ_B is the Schottky barrier height of the metal/semiconductor pair, which in the Anderson model without interface charges is given by the difference between work function of the metal and electron affinity of the semiconductor. Φ_{nF} is the potential difference between conduction band and Fermi level. The device is called a metal-semiconductor-metal (MSM) diode because the backside contact is an ohmic metal contact. MSM photodiodes have the advantage of easy technological realization but suffer from high dark currents. The high dark currents are caused by the lower built-voltage V_{bi} of Schottky contacts compared to p/n junctions, for example, in Si, 0.3–0.6V versus 0.8–1 V. To solve the dark current problem, a thin insulating layer is placed between the metal and the semiconductor. This junction is called MIS, or it is called MOS if the insulator is silicon oxide. The insulating oxide separates the depletion layer from the gate metal contact. We have the same work function difference like in an MSM diode, but now part of the potential difference drops across the insulator (V_i). The potential difference along the depletion layer is now governed by the surface potential Ψ_s, which replaces ($V_{bi} - V$) given for p/n and Schottky photodiodes in Eqs. 9.15–9.20.

Consider a p-type substrate without interface charges. The work function difference is described by the flat band voltage V_{FB}. The surface potential Ψ_s is given by

$$\Psi_s = -V_{FB} + V - V_i, \tag{9.22}$$

where

$$V_i = |Q_s| d_i/\varepsilon_i. \tag{9.23}$$

Here Q_s is the total charge in the semiconductor depletion layer and d_i and ε_i are the thickness and the dielectric constant (permittivity), respectively, of the insulator. Ideally, the flat band voltage V_{FB} is defined by the work function difference between metal and semiconductor. Corrections have to be made in the case of oxide charges. The voltage drop across the insulator is given by V_i. The depletion layer into the semiconductor is described by the same equations (Eqs. 9.17 and 9.18) as before but the potential difference ($V_{bi} - V$) in the p/n junction is now replaced by the surface potential Ψ_s. In MOS varactor or transistor operation two additional modes are available, inversion and accumulation. A positive gate voltage higher than the so-called threshold voltage V_{th} (in our example of a p substrate) induces a thin n-layer—the n-inversion channel—below the oxide. A negative voltage below the flat band voltage V_{FB} removes the depletion layer and induces a majority carrier increase (p accumulation) of the oxide interface. The conventional n-channel MOS transistor operates between inversion (on: the n channel is connected to the n-doped source + drain regions) and the depletion (off). The gate insulator should be thick enough (silicon oxide thicker than about 3 nm) to avoid significant tunneling currents. The MIS photodiode operates differently. There are no connections to source/drain regions, and the insulator is thin enough to allow tunneling of carriers. Figure 9.9 shows a typical arrangement for MIS photodiodes for vertical light incidence [6]. For simplicity, the backside contact is shown on the substrate backside. In integrated circuits, the backside contact is placed on the front side and connected to the device by a highly doped buried layer.

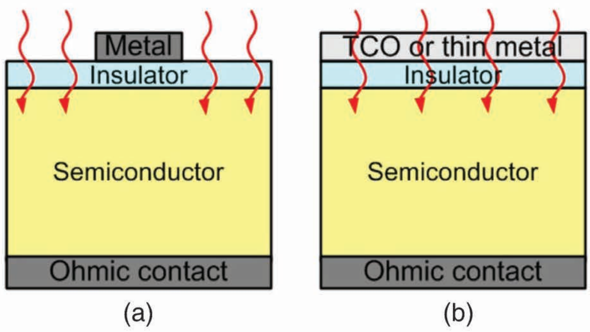

Figure 9.9 The schematic structures of MIS photodetectors [6]. (a) Light radiates into the semiconductor from the unshadowed region when the metal is not transparent. (b) Light radiates into the semiconductor passing through the transparent conducting oxide (TCO) or thin semitransparent metal film. Reproduced under open access (CC BY) from Ref. [6] (https://www.mdpi.com/openaccess).

A normal metal gate shadows the incident vertical light (Fig. 9.9a) so that absorption takes place only around the metal finger. A preferred embodiment of the MIS uses transparent gate electrodes (Fig. 9.9b), either a thin semitransparent metal film or a transparent conducting oxide. The current mechanisms of an MIS diode are shown in Fig. 9.10. An inversion bias (positive for a p substrate) is applied. In Fig. 9.10a, the dark current is shown.

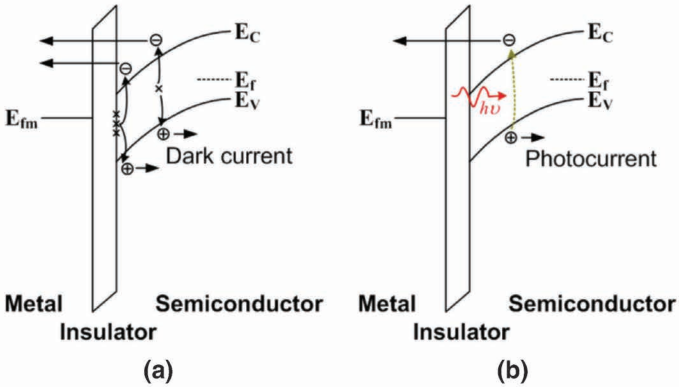

Figure 9.10 The current mechanisms of an MIS diode [6]. (a) Without light incidence; (b) with light incidence. A positive bias (inversion bias) is applied for this metal/insulator/p-type semiconductor example. Reproduced under open access (CC BY) from Ref. [6] (https://www.mdpi.com/openaccess).

Although an inversion bias ($V > V_{\text{th}}$) is applied, no inversion layer is created in the MIS photodiode! This is because the inversion channel in an MIS diode is built up by minority carriers generated in the depletion region. In the MIS photodiode these minority carriers leak through tunneling to the gate and define the dark current of the device (Note: In an MOS transistor the inversion channel is fed by the highly doped source/drain regions. This explains the much higher dark current in transistors with thin, leaky insulators). Absorption of light (Fig. 9.10b) adds hole-electron pairs that are separated by the electric field of the depletion layer and measured as photocurrent. Forward bias shifts, however, the metal Fermi level above the semiconductor conduction band, which results in strong electron tunneling from the metal side to the semiconductor, delivering a high current with near-ohmic contact properties. This operation mode is used in interdigitated contact fingers to create both contacts of the photodiode at the front side of the chip (metal-insulator-metal).

9.3.3 Avalanche Photodetector

An integrated or external low noise amplifier, as discussed with the active CMOS pixel, may amplify the photocurrent. Alternatively, an internal amplification mechanism may be sought. The most important physical mechanism for internal amplification is impact ionization in a strong electric field, which causes avalanche multiplication. The maximum electric field $\vec{F}_{\mathrm{m}}$ at which avalanche breakdown onsets depends on the material and on the length where multiplication takes place. The maximum field $\vec{F}_{\mathrm{m}}$ is smaller in semiconductors with low bandgap energies. The electric field extends to the lower doped region in a one-sided abrupt junction. To give an example, the maximum field $\vec{F}_{\mathrm{m}}$ in Si doped to $10^{17}/\mathrm{cm}^2$ ranges to about $6*10^7$ V/m. Avalanche photodetectors (APDs) from III/V materials are widely used in high-bit-rate, long-haul optical communication systems. Compared to their p-i-n counterparts, APDs can offer better sensitivity due to their internal multiplication gain [7]. For one key figure of merit—the ionization ratio between holes and electrons—the silicon is superior to most other semiconductors. A small ionization ratio (as in Si) affects important properties like sensitivity, excess noise, and gain-bandwidth product advantageously. This is important because avalanche multiplication is a noisy process and care has to be taken that the noise floor is not increasing more than the photocurrent. Combining the good avalanche properties of Si with the absorption of different semiconductors led to heterostructure APDs.

Heterostructure APDs employ a separate absorption-charge-multiplication structure in which light is absorbed in an intrinsic heterostructure film while carriers are multiplied in the high field region of the Si film. In a Si/Ge-heterostructure APD the intrinsic absorber region is made from Ge whereas the multiplication is often made in a Si p-i-n structure. The multiplication structure consists of a thin p charge layer, a thin intrinsic multiplication layer, and an n charge layer. This high-low-high doping structure is well known in high-frequency IMPATT diodes for providing a spatially uniform avalanche multiplication rate. The full layer sequence on a Si substrate consists of an n^+-Si contact layer, an i-Si multiplication layer, a p-Si charge layer, an i-Ge absorption layer, and a p^+-top contact layer [7]. The frequency-gain product gives a characteristic performance number of APDs. In Ge-on-Si APDs, frequency-gain values of 300 GHz can be obtained with a gain of 15 and a 3 dB frequency limit of 20 GHz.

9.4 Spectral Range

The spectral range of bulk silicon stretches from the VIS to the UV. The absorption depth in UV is very short (order of magnitude 10 nm), so near-surface collection, for example, in MIS structures is necessary. This spectral range is extended to the NIR by using Ge/Si heterostructures. A further extension beyond 1.55 μm can be expected with progress in GeSn/Si heterostructures. α-Sn is a zero bandgap semiconductor. The alloy GeSn shifts the bandgap to lower values than that of Ge (0.66 eV). This material is not stable under equilibrium; sophisticated growth and device processing is necessary to exploit the NIR properties of metastable GeSn alloys.

An extension to the MIR and FIR seems not possible with bulk silicon–based materials. However, quantum size effects may be used to extend the spectral range [8–11] into the FIR. Quantum size structures like quantum wells (QWs), quantum wires, and quantum dots (QDs) break up the bands into sub-bands with quantum number $n = 1, 2 \ldots$ (Fig. 9.11).

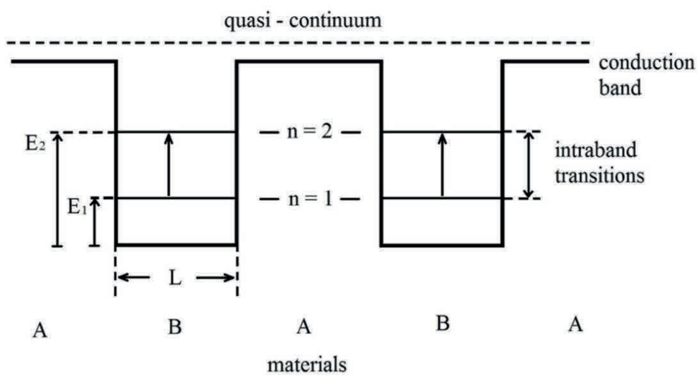

Figure 9.11 Heterostructure quantum well created by materials A/B. Shown is the conduction band (with B as lower-electron-energy material). In the quantum well electron substrates with energy edges E_1 and E_2 are created. Transitions between E_1 and E_2 are called intraband transitions.

The energies of a rectangular well are given by

$$E_n = (\hbar^2\pi^2 / 2m^* L^2)n^2 \tag{9.24}$$

for a well with an infinite barrier. Here m^* is effective mass, L is well width, n is quantum number, and $\hbar = h/2\pi$ is reduced Planck's constant.

To give an impression of a typical quantization energy, let's consider a well width L = 12.5 nm, and an effective mass of 0.19 m_0 (Si: transverse electron mass; m_0 free electron mass). Then we obtain E_1 = 12 meV and E_2 = 48 meV, and the intraband transition $E_1 - E_2$ would be 36 meV (corresponds to about 30 μm wavelength). So, silicon-based photodetectors may cover the whole spectral range if we include Ge/Si heterostructures and quantum size structures. The competition with other materials is especially hard in the UV (wide bandgap semiconductors), NIR (ternary III/V compounds), and FIR (small bandgap semiconductors or other device principles, like photoconduction and bolometer) range. Next we will cover the different parts of the spectrum, with a strong emphasis on NIR.

9.4.1 UV Detectors

UV light is usually divided into three wavelength regions: UV-A (320–400 nm), UV-B (280–320 nm), and UV-C (10–280 nm). UV light is harmful to human beings. It can be used in chemical and biological processes, and very hot objects (stars, rockets, etc.) and processes (welding, etc.) emit UV rays. The main applications of UV detectors are therefore in environmental, chemical, and biological analysis and in astronomy, military, and industry. The very near surface absorption is best handled with MIS photodetectors. The thin metal gate may be used as a filter. A VIS-blind design for the detector is desired because usually VIS light is hiding weaker UV emissions. An interesting demonstration was given [12] with silver gate metals as a filter having a window of around 320 nm. Ag films of thickness 70–130 nm block VIS light, whereas responsivities around 10 mA/W could be obtained at 320 nm.

9.4.2 Visible Spectrum

The VIS spectrum is the most competitive part of bulk silicon detectors. Charged coupled device–based or more recently CMOS–

based detector arrays are virtually ubiquitous in mobiles, webcams, home entrance, and security equipment. A huge industry has emerged by joining microelectronics and optoelectronics on silicon substrates. The pixel schemes are already shown in Section 9.1. Most of these detectors use a large absorption volume, which limits speed to the 100 MHz frequency region.

With SiGe/Si or Ge/Si heterostructures the photodetectors show improved frequency behavior even in the VIS spectrum. The reason is the higher absorption, which allows smaller devices.

9.4.3 NIR Spectrum

Ge on Si photodetectors are the first choice to extend the spectral range to the telecommunication wavelengths 1.3 μm and 1.55 μm. The first high-performance Ge-on-Si photodetectors were normal incidence devices for free space or optical fiber coupling. We simplify in Fig. 9.12 those parts of the band structure in Si and Ge that are responsible for NIR absorption.

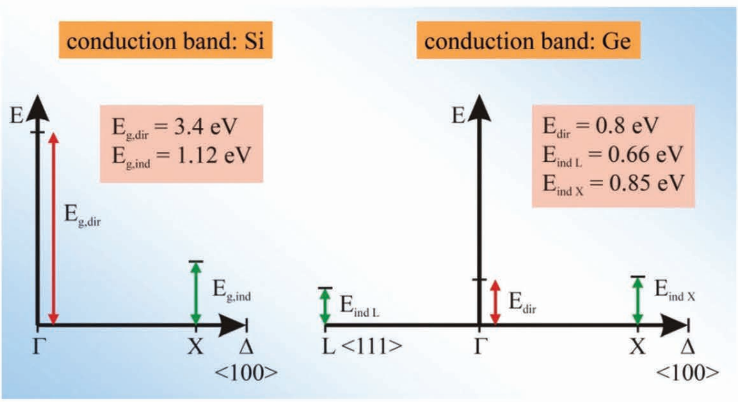

Figure 9.12 Simplified scheme of the conduction band minima in Si and Ge. Given are the energies for direct and indirect transitions. Reprinted by permission from Springer Nature Customer Service Centre GmbH: Springer Nature, *Frontiers of Optoelectronics in China*, Ref. [1], copyright (2010).

The lowest direct transition in Si is 3.4 eV (360 nm) above the valence band, whereas in Ge this direct transition comes down to 0.8 eV (1.55 μm). That means all the absorption in the VIS spectrum is indirect in Si whereas from the NIR through the VIS range, the absorption in Ge is direct. This makes Ge superior in optoelectronics in the NIR and VIS range. The lowest indirect transition in Si is the Δ minimum (Δ is near the X point, 0.8X in Si), with a gap of 1.12 eV (room temperature). In Ge the Δ minimum is at 0.85 eV, but the lowest minimum is now at the L point (111), with 0.66 eV. In unstrained Ge the Δ minimum is of small significance but in compressively strained Ge, the difference to the L minimum shrinks that in fully strained Ge on Si the Δ minimum wins (Si like conduction band structure). Note that practically fully strained Ge on Si can only be obtained for a few-nanometer thickness because of strain relaxation in highly mismatched heterosystems. A basic structure of a Ge photodiode is shown in Fig. 9.13.

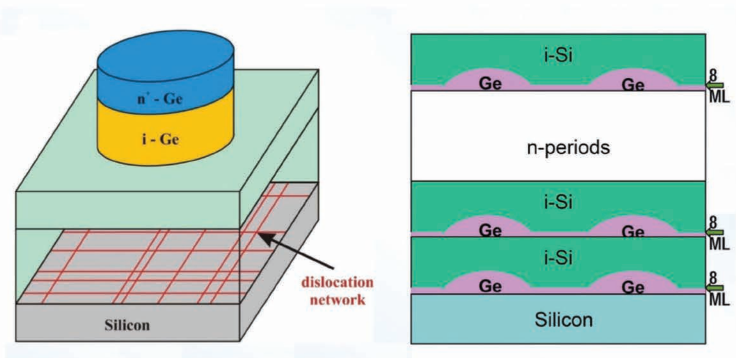

Figure 9.13 Basic structure of Ge p-i-n photodetectors on Si substrates. Left: A strain-relaxed Ge buffer layer accommodates the lattice mismatch by a dislocation network at the Si/Ge interface. Right: Ge islands arranged in planes with Si spacers (Ge-dot superlattice).

Here you see on the left a typical structure with a strain-relaxed buffer (SRB) of Ge on the Si. As a result, a dislocation network is created at the interface to the Si substrate. The combination of Si substrate and SRB is called a virtual substrate, which offers on top of a common Si substrate a different lateral lattice spacing, in this case the spacing of Ge. This virtual substrate concept is very flexible, but rather high threading dislocation densities (10^5–10^8 / cm^2) plague it. The best Ge SRBs (graded buffer) need to be about 10 μm thick, which is hardly acceptable for integrated circuits. Much more limited is the Ge amount in an approach (Fig 9.13, right) that prevents dislocations. Strain may be relaxed by surface corrugations or even better by island formation. Repeated growth of Ge island layers interrupted by Si (Ge-dot superlattice) allows dislocation-free absorber structures (as mentioned with low Ge amounts corresponding to 10–50 nm Ge layer thickness).

A sketch of a technical realization [13, 14] of a Ge photodiode is shown in Fig. 9.14.

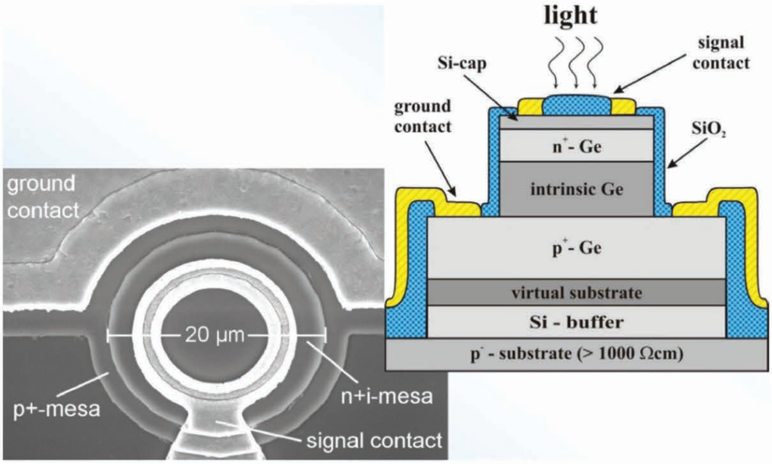

Figure 9.14 Top view (left) and cross section (right) of a Ge photodetector on a virtual substrate. © 2005 IEEE. Reprinted, with permission, from Ref. [13]. Reproduced from Ref. [14], with the permission of AIP Publishing.

On top of the virtual substrate (Si + relaxed Ge) a p-i-n structure is grown starting with a p$^+$-Ge (used as backside contact), then followed by the intrinsic Ge as the absorber layer and an n$^+$ top contact layer. For processing purposes the n$^+$-Ge top layer is covered by a thin Si cap. The top contact metal is a ring, which should be transparent in the middle for light incidence. A double-etched structure allows backside contact from the frontside and connection to high-speed CPW measurement pads. The dark current of Ge junctions is 6–7 orders of magnitude higher than in Si because of the smaller bandgap. In Ge bulk diodes current densities of 10 µA/cm^2 will be obtained. In heterostructure diodes, the dark currents [15] are usually higher because of defects (dislocations, point defects, etc.), high contact doping (Auger recombination), and thin contact layers. Figure 9.15 shows the I–V characteristics of Ge-on-Si diodes with an absorber region of different thicknesses d_i.

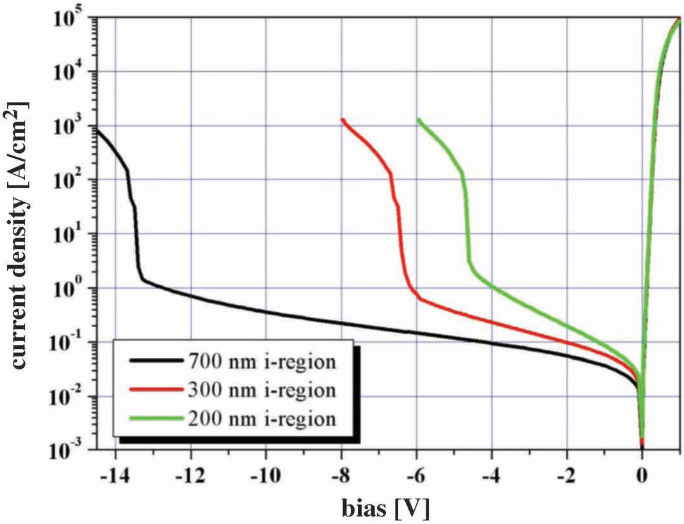

Figure 9.15 Dark current density versus bias voltage of Ge-on-Si photodiodes with different thicknesses of the intrinsic layer.

For a negative bias the reverse characteristics are shown. One sees the increase of the reverse current with a negative bias until the onset of avalanche multiplication. This onset depends on the thickness of the i-layer: −13.5 V, −6.2 V, and −4.5 V for layer thicknesses of 700 nm, 300 nm, and 200 nm, respectively. Another effect typical for defect-dominated recombination can be seen: the increase of dark current with thinner layer structures. This is typical of tunneling-assisted generation of currents from defect levels. Tunneling increases the generation as a function of the applied field. The dark currents are very similar if they are considered as a function of the field strength in the absorption layer (Fig. 9.16).

This dependence on field strength can be considered as a proof of defect level–dominated dark currents [15]. Avalanche multiplication follows the rule that breakdown field is lower in thicker layers (at lower fields the avalanche needs a longer distance for proper impact ionization).

The responsivity R (do not confuse with reflectivity) of a Ge detector is given by

$$R = R_{\text{opt}} \times \eta_{\text{int}} \times \eta_{\text{ext}}, \tag{9.25}$$

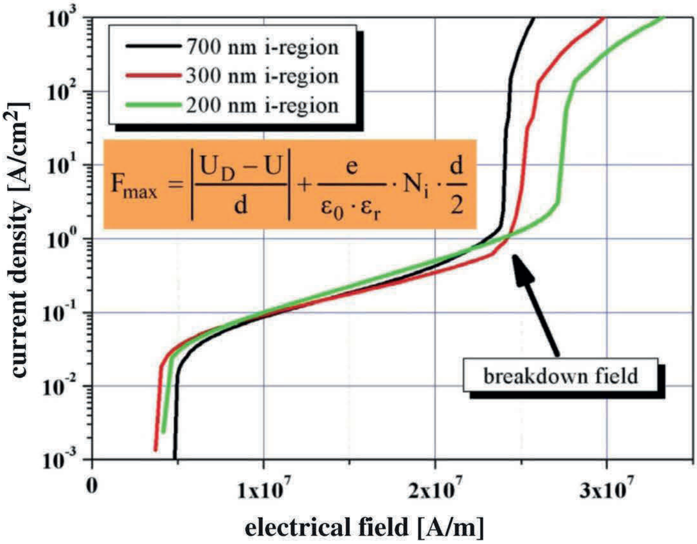

Figure 9.16 Electrical field dependence of defect-dominated dark currents in Ge-on-Si photodiodes.

with optimum responsivity R_{opt} (A/W) given by

$$R_{\text{opt}} = q / \hbar\omega = \frac{q}{hc}\lambda = \lambda(\mu\text{m}) / 1.24. \qquad (9.26)$$

The real responsivity is reduced by a nonideal internal quantum efficiency ($\eta_{\text{int}} < 1$) and by an external efficiency ($\eta_{\text{ext}} < 1$), which is caused by reflections and absorption in top layers [16]. A typical example of the spectral responsivity of a Ge photodiode with submicron absorption layers (thickness d_{i}) is shown in Fig. 9.17.

A large dark current degrades the signal-noise ratio. A figure of merit is the normalized detectivity D^* [17].

$$D^* = \sqrt{A \Delta f} \,/\, \text{NEP}, \qquad (9.27)$$

where A is area, Δf is bandwidth, and NEP stands for noise equivalent power. In the case of shot noise from the dark current I_{d} [18] the NEP reads $(2eI_{\text{d}}\Delta f)^{1/2}/R$, which results in a normalized detectivity

$$D^* = \sqrt{A} \cdot R_{\text{opt}} \,/\, (2eI_{\text{d}})^{1/2}. \qquad (9.28)$$

The detectivity improves with responsivity and degrades with high dark currents. It is, therefore, important to operate the photodiode under low dark current conditions. As the dark current of Ge diodes is rather high, this means operation under a low reverse bias. The ideal answer would be operation under zero bias (solar cell mode).

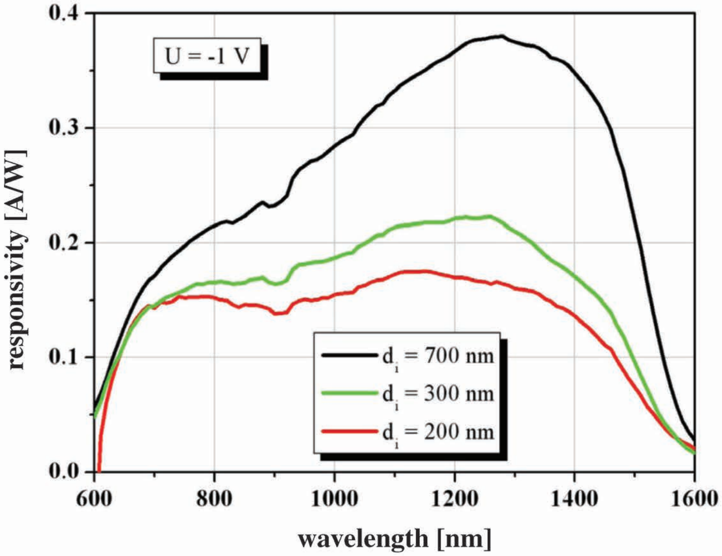

Figure 9.17 Spectral dependence of responsivity of Ge-on-Si photodiodes with different intrinsic layer widths. Republished with permission of Electrochemical Society, Inc, from Ref. [16] (1948); permission conveyed through Copyright Clearance Center, Inc.

Not only does a zero-bias operation [19] optimize detectivity, it is also beneficial for low power consumption in a stand-by modus. At this point it can be stated that the uncritical use of dark currents at a given voltage (mainly 1 V is used) is a measure of layer quality. As shown before, the dark current depends on the electrical field, which is higher in thinner layers. At the same material quality, the dark current at a fixed voltage increases with decreasing thickness. An exact measure delivers dark current versus electric field, but a rapid quality-correlated measure (number and emission properties of defect levels) would be dark current divided by thickness. For detectivity, it is crucial to find the lowest voltage for full speed operation of the photodiode.

Figure 9.18 shows the bias voltage dependence [20] of photocurrents for different optical power inputs.

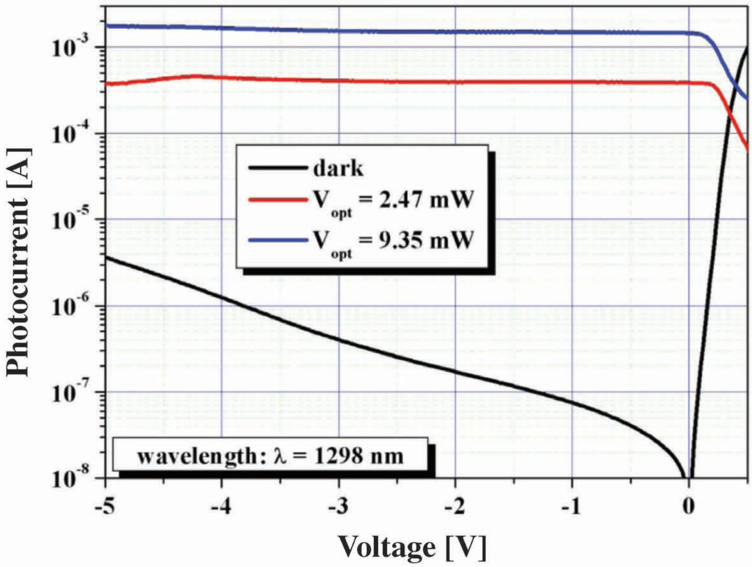

Figure 9.18 Bias voltage dependence of the photocurrent of a Ge p-i-n photodiode with 700 nm intrinsic width of the p-i-n structure. Reprinted from Ref. [20], Copyright (2009), with permission from Elsevier.

It is clearly seen that the photocurrent and, therefore, the responsivity is constant through the reverse bias (λ = 1.3 μm), at zero bias, and even within a small regime of forward bias [21]. This is a typical property of a p-i-n diode with a fully depleted i-region. Constant responsivity throughout the complete reverse bias regime does not mean that the high-frequency response stays conserved, but that is a topic of the next section in this chapter.

We have shown that for Ge p-i-n photodiodes [16] with low background doping ($<3\cdot10^{15}$ cm^{-3}) a zero-bias operation is possible. The responsivity curve is independent of reverse bias at λ = 1.3 μm, and this holds true for all wavelengths except the near-band-edge absorption around 1.55 μm. Here, an electro-optical effect—the Franz–Keldysh effect—modulates the absorption coefficient near the band edge with increasing field strength (Fig. 9.19).

In Fig. 9.19 $(R_{opt}/\lambda)^2$ is depicted against photon energy. In a direct semiconductor approximation for thin layers this should be a linear function near the band edge, as demonstrated in Fig. 9.19. With an increasing electrical field, the slope of the curve decreases and absorption below the direct bandgap increases. This effect is also used in absorption modulators, and details are discussed there.

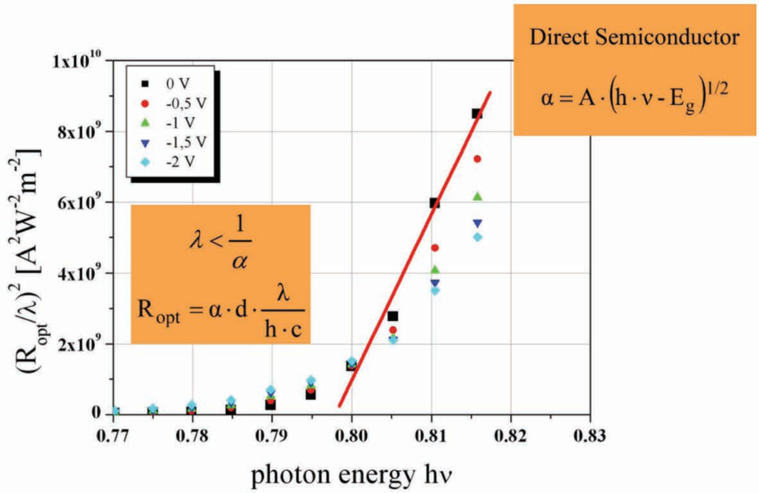

Figure 9.19 Franz–Keldysh effect in Ge-on-Si p-i-n photodiodes. Reprinted from Ref. [22], Copyright (2012), with permission from Elsevier.

We discussed the behavior of Ge-on-Si detectors for vertical incidence. The basic properties are similar for lateral waveguide incidence, with two added advantages that stem from the fact that the absorption length is now decoupled from the absorption layer thickness d_i. The length l_i of the absorption layer can be fabricated within a few micrometers to a few tens of micrometers whereas the thickness d_i stays at submicron values to facilitate monolithic integration. Two big advantages result from this decoupling: The quantum efficiency at the band edge (1.55 μm) can be increased from below 10% to nearly 100%. The design of high speed (strongly dependent on d_i) and the design of high responsivity (now dependent on l_i) can be optimized independently.

The first successful realization of a SiGe/Si-waveguide detector dates back to 1994 [23]. A bulk Si substrate with a ridge SiGe waveguide was used to couple in the wave (1.3 μm) into a pseudomorphic SiGe/Si superlattice detector (Fig. 9.20).

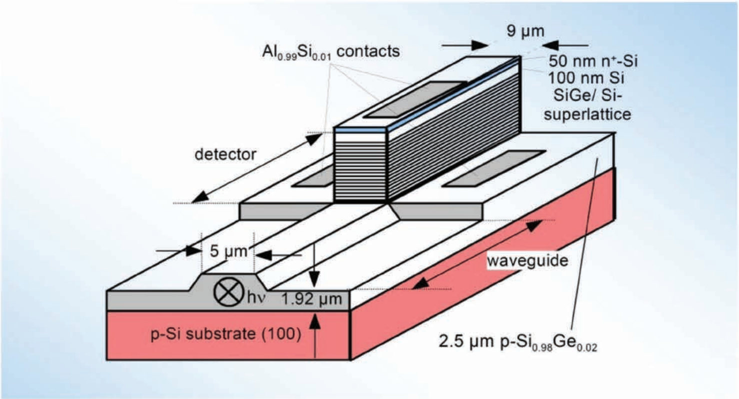

Figure 9.20 Waveguide photodetector. A rib of SiGe on Si forms the waveguide. A SiGe/Si superlattice photodiode detects the 1.3 µm light. © 1994 IEEE. Reprinted, with permission, from Ref. [23].

In the given example there is evanescent coupling from the underlying waveguide to the detector. This is possible because of the higher index of refraction of Ge leading the wave into the detector. The alternative coupling is direct butt coupling with waveguide and detector face-to-face (Fig. 9.21).

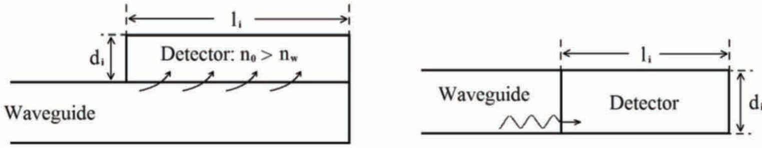

Figure 9.21 Waveguide-detector coupling. (a) Evanescent coupling mode and (b) Butt coupling.

Recent success in Ge/Si APDs with internal amplification led to a revival of this long-known device concept, which has to prove competitiveness with separate amplification with modern low noise amplifiers [6].

Ge/Si APDs have been successfully fabricated by blanket epitaxial Ge growth or selective Ge growth on epitaxial Si films [24–26]. During Ge/Si APD fabrication, a 50–100 nm p-Si charger layer can be formed either by ion implantation into the epitaxial i-Si layer or by in situ doping. Other processing techniques are similar to Ge p-i-n diodes discussed earlier.

Although the gain-bandwidth product is commonly used in literature to characterize APD performance, sensitivity more completely characterizes the overall figure of merit, which reflects the relationship between a gain-bandwidth product, responsivity, excess noise, and dark current. The theoretical sensitivity of 10 Gb/s Ge/Si APDs at a bit-error rate (BER) = 10^{-10} is a function of gain (M) for different primary dark currents (I_{DM}) [27]. Ge/Si APD receiver sensitivity is theoretically better than that of commercial III/V APD receivers (–28 to –26 dBm) [7] if optimum responsivities and a typical transimpedance amplifier noise of 1 μA are assumed.

There are two approaches to improve Ge/Si APD sensitivity: (i) reduce the primary dark current below 100 nA and (ii) enhance the primary responsivity to the commercial III/V APD level (>1.8 A/W). Similar to waveguide-coupled Ge p-i-n diodes, waveguide-integrated Ge/Si APDs offer advantages in low absolute dark current and high bandwidth-efficiency product. Recent waveguide-integrated Ge/Si APDs successfully demonstrated –31 dBm sensitivity at 1.3 μm and BER = 10^{-10} [24].

9.4.4 SiGe/Si Quantum Dot (Well) IR Photodetectors

Due to the natural valence band offset at the SiGe/Si heterojunction, discrete energy levels form inside the Si/SiGe/Si quantum confinement region. The transition between these discrete levels can be used for infrared detection [8, 11]. The SiGe/Si quantum-dot structure has been fabricated into MIS SiGe/Si QD infrared photodetectors (QDIPs) [28]. SiGe QDs were formed on a Si substrate by the Stranski–Krastanov mode [29]. It is worth mentioning that the gate electrode selected here is Al instead of Pt because for the SiGe/Si QDIP structure, the semiconductor is p-type and Pt will lead to a hole tunneling current at the inversion (positive) bias [30], which should be avoided.

The insertion of an insulator layer to fabricate the MIS photodetector indeed could reduce the dark current. For MIS SiGe/Si QDIP, the thermionic emission current of holes from Al to the semiconductor was significantly reduced due to the extra barrier and the suppression of Fermi-level pinning with an insulator layer. Boron δ doping combined with QW or QD is often used for technical realizations [31, 32].

9.5 High-Speed Operation

Usually, Si detectors are slow because they rely on the large diffusion lengths in high-quality Si. However, diffusion is a rather slow process from the random walk of carriers in the electric-field-free part of the diode. Let us now concentrate on the reason for the rapid increase of speed of Ge/Si photodetectors from the 100 MHz regime into the low millimeter-wave regime (30–50 GHz) within a few years [33–39]. The measurement by the S-parameter network analyzer includes the speed of the detector and the delay caused by the laser light modulator, so the real speed of the detector is somewhat higher, about 60–80 GHz. The essential contribution stems from the reduced device size of Ge photodiodes, which minimizes carrier transit times. An additional important measure is to suppress the slow minority carrier diffusion from absorption outside the depletion layer (Fig. 9.22).

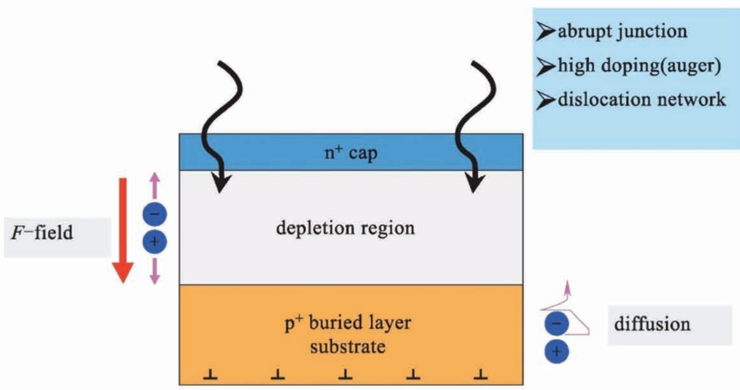

Figure 9.22 Suppression of the slow carrier diffusion from outside the depletion region.

This is accomplished by a combination of three technological steps:

1. Very abrupt junction. Transition of the highly doped contact layers to the intrinsic layer (several orders of magnitude difference in doping) is within a few nanometers. The abrupt transition confines the electric field to the intrinsic layer.
2. High doping ($>10^{20}$ cm^{-3}) of the contact layers to reduce carrier lifetime by the Auger effect. A short carrier lifetime

causes a short diffusion length, which minimizes current contributions from slow diffusion.

3. A misfit dislocation network at the bottom contact that reduces the lifetime of minority carriers. Lattice defects like dislocations push the recombination of carriers. This stops the unwanted slow diffusion of minority carriers from the bottom contact if the misfit dislocation network is outside the depletion region. (Note: Threading dislocations, which cross the depletion layer, enhance the dark current by generation of carriers in the high electric field of the depletion layer). The diffusion length L of minority carriers is given by

$$L^2 = D\tau = q\mu\tau. \tag{9.29}$$

Here q, D, μ, and τ are the electric charge of the electron, the diffusion coefficient, the mobility, and the minority carrier lifetime, respectively.

At high doping, the diffusion length is reduced by the low mobility (a factor of 30 lower than in undoped material). The low minority carrier lifetime of high-doped semiconductors is caused by the Auger effect, where the momentum of the recombining electron (hole) is transferred to a nearby available electron (hole). As a result, the diffusion length L shrinks from more than 10 μm in a low-doped material to below 0.1 μm in high-doped layers.

Two effects dominate the detector speed if the slow diffusion is suppressed.

- The internal speed of the device is given by the transit time. Assuming a saturation velocity v_s of carriers in the depletion region, the internal frequency band f_{tr} is given by the simple expression [14]

$$f_{tr} = \frac{\sqrt{2}}{\pi}\frac{v_s}{w_D}, \tag{9.30}$$

  where v_s and w_D are the saturation velocity ($v_s = 0.6 \times 10^5$/s in Ge) and drift width (the intrinsic width in abrupt junctions), respectively.

  The assumption of saturation velocity is correct if the field strength $\vec{F}$ is more than about 3×10^6 V/m (e.g., with $V_{bi} - V =$ 1 V, $w_D = 300$ nm, and the field strength $\vec{F} = 3 \times 10^6$ V/m).

- The connection to the outer world (measurement surrounding) is limited by the RC load given by the capacitance C_j of the device and by the resistance of the connection line (R_S + 50) Ω (R_S is the series resistance; 50 Ω is the waveguide measurement impedance):

$$f_{RC} = \frac{1}{2\pi RC_j} = \frac{1}{2\pi} \cdot \frac{w_D}{A\varepsilon(R_S + 50)} \tag{9.31}$$

The 3 dB bandwidth f_{3dB} is roughly given by a superposition [14]:

$$\frac{1}{{f_{3dB}}^2} = \frac{1}{{f_{tr}}^2} + \frac{1}{{f_{RC}}^2} \tag{9.32}$$

The influence of the RC load is shown in Fig. 9.23, where a 50 GHz internal speed detector is loaded with different capacitances C_j.

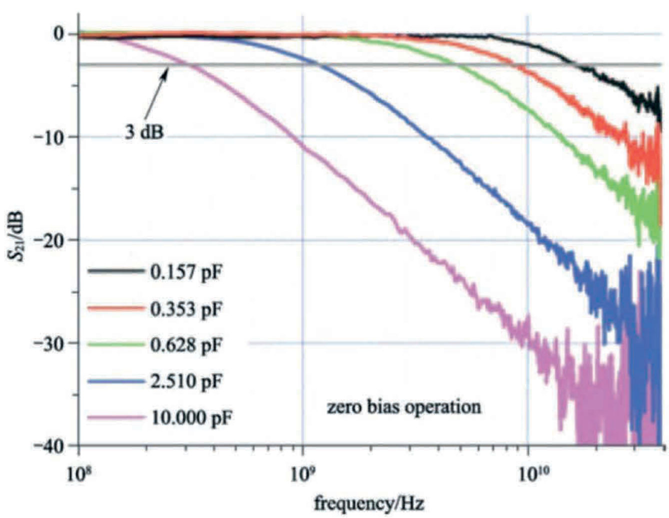

Figure 9.23 Response versus frequency for differently loaded detectors of the same internal structure (50 GHz internal speed). Reprinted by permission from Springer Nature Customer Service Centre GmbH: Springer Nature, *Frontiers of Optoelectronics in China*, Ref. [1], copyright (2010).

From these investigations, we concluded the dependence of vertical detector speed [13, 14] on the thickness of the intrinsic zone and the device mesa radius (Fig. 9.24).

The results demonstrate that with small pixel devices (4 μm diameter), speeds far above 100 GHz should be obtained readily for 100 Gbit/s detection.

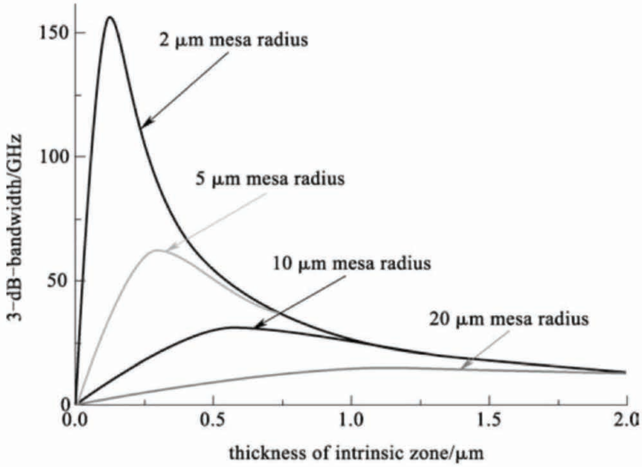

Figure 9.24 Theoretical 3 dB bandwidth of vertical Ge/Si photodetectors [14].

The speeds of properly designed Ge-on-Si detectors is already obtained at low reverse biases (Table 9.3). Ge is a small-bandgap semiconductor that is always connected with much higher dark currents than usual in Si. To minimize dark currents, operation of the device at zero bias is highly appreciated. Our group obtained very good results with a zero-bias operation [13, 33] due to the very abrupt junctions grown by molecular beam epitaxy (MBE).

Table 9.3 Three dB frequencies f_{3dB} of photodetectors (compared are detectors with reverse-bias and zero-bias detectors)

Organization	Bias/V	f_{3dB}/GHz	Wavelength/nm	Remark
IBM [39]	−4	29	850	Reverse bias
MIT [34]	−3	12.1	1540	„
LETI [35]	−2	35	1310/1550	„
USTUTT [13]	−2	39	1550	„
LUXTERA [36]	−1	> 20	1554	„
LETI [37]	−4	42	1550	„
ETRI [38]	−3	35	1550	„
USTUTT [33]	−2	49	1550	„
USTUTT [13]	0	25	1550	Zero bias
USTUTT [33]	0	39	1550	„

9.6 Outlook

Ge is a small-bandgap semiconductor with much higher dark currents than usual in Si. Recent activities with heterostructure photonic devices aim to perform competitively with photodiodes from III/V materials with the advantage of relying on sophisticated technologies from Si microelectronics. Four technological efforts have mainly contributed to the progress in Ge-on-Si photodetector performance.

These performance drivers are:

- A well-balanced trade-off of key properties by improving the responsivity at the band edge of Ge, by reducing the dark current, and by improving the linearity without compromising too much the speed.
- Extension of the wavelength window toward the MIR by using novel heterostructures that are metastable available at nanometer dimensions.
- Exploiting lateral entrance of light in waveguide geometries by carefully designed contact geometries.
- Foundry service offered for material and device technology of Ge-on-Si photonics. This allows more groups to bring in their special knowledge of photonics, and it improves the precision and reliability of processing.

The absorption of unstrained Ge decreases strongly near the direct-bandgap-cutoff wavelength of 1.55 μm. The responsivity increases, and the cutoff wavelength extends to more than 1.6 μm using tensile-strained Ge [7] with a low strain level (about 0.25%). This small strain level is simply obtained by annealing a strain-relaxed Ge-on-Si. A thermal expansion mismatch causes the tensile strain because the thermal expansion coefficient of Ge is larger than that of the Si substrate. Alternatively, a strain-relaxed GeSn buffer with small Sn amounts (1–2%) can be used if the anneal temperatures (750°C–850°C) do not fit into the process sequence. Multiple reflections enhance the absorption length, which is beneficial for vertical incidence devices. Technical solutions range from bottom-side oxide mirrors [34] to resonance cavities (resonance-cavity-enhanced photodetector) realized by dielectric Bragg reflectors on the front and bottom [40]. Light scattering on surface corrugation delivers a longer pathway in the absorber, as has already been demonstrated in solar cells. Application to photodiodes delivers a technologically simple route for responsivity enhancement [41]. The black silicon light-trapping structure can be applied to the device's rear during back end processing.

The most demanding improvement regarding detectivity concerns the dark current of Ge-on-Si photodiodes. The ideal dark current of semiconductor p/n junctions increases with small-bandgap materials, but the real dark currents of strain-relaxed structures are usually orders of magnitude higher because of defects correlated with the lattice mismatch accommodation. The dark current is mainly caused by recombination of carriers at threading dislocations and point defects correlated with dislocation climb and low growth temperatures. Carefully chosen epitaxy processes and dangling bond passivation by hydrogen have the potential to reduce the dark current densities from the order of 100 mA/cm^2 to below 1 mA/cm^2. The benchmark value for dark currents is set to 0.8 mA/cm^2 with small-bandgap III/V-epitaxy on Si substrates [42]. Space charge effects within the depletion region limit the output power of photodiodes. At high photocurrents, the linearity of the device suffers from the injection of carriers, which influences the electric field distribution. A specific doping profile in unitravelling carrier photodiodes improves the linearity to larger 1 dB saturation photocurrents [43] than available in p-i-n diodes.

Extension of the wavelength regime into the MIR is not possible with stable bulk Ge compounds. One needs either metastable GeSn alloys or highly strained Ge that is stable only in nanoscale structures. Both Sn alloying to Ge and tensile strain reduce the direct bandgap and shift, thereby, the responsivity of photodiodes beyond the 1.55 μm wavelength into the infrared region. In parallel, these material modifications reduce the energy distance between direct and indirect bandgaps. From the latter property, light emitters like LED and laser benefit whereas the first property pushes photodetectors' wavelength range. Of utmost importance is, however, that the same technological measures support detectors and light sources. A more detailed description is given in Chapter 12. It is reasonable to expect first demonstrations of Si-based monolithic integrated photonic systems in the 1.5–2.5 μm wavelength range. The progress in material science [44] is key to getting there. In essence, two challenges face heterostructures on silicon. The most obvious is the lattice mismatch, which amounts to 4.2% for Ge on Si and to 17.4% for Sn on Ge. The lattice mismatch is below 5% for Ge-rich GeSn (Sn amount below 25%) on Ge, which is similar to SiGe/Si. Under equilibrium, high strain values are only obtained for very thin layers of a few nanometers. High strain values for thicker layers need nonequilibrium fabrication steps conserving metastable structures. Heterostructures of GeSn on Si or on Ge rely completely on metastability because the mixture of Ge and Sn breaks up into two alloy compositions under equilibrium. Fabrication at very low temperatures (below 500°C) is essential. Several approaches rival for future photonic system solutions at wavelengths beyond 2.5 μm [45]. Sharpness and defect structure of interface transitions [46] play a significant role in the optical properties of 2D (QWs), 1D (quantum wires), and 0D (QDs) heterostructures. Photodetectors from GeSn on a virtual Ge substrate are on the way toward MIR application, pending further improvement in material quality to reduce the dark current [47]. Strain-relaxed GeSn alloys with Sn amounts of 4.5% and 9.5% are needed to reduce the direct bandgap transition from 0.8 eV to 0.65 eV and 0.5 eV, respectively. The same bandgap reduction will be obtained with biaxial, tensile strain of 1% and 2%, respectively. Unfortunately, compressive strain results from the straightforward growth of GeSn-on-Ge virtual substrates, which requires high Sn amounts (>10%) for detectors with wavelengths beyond 2.5 μm. As mentioned, low-dimensional nanostructures point toward metastable GeSn alloys of good quality. Core/shell nanowires with a Ge/GeSn [48] heterostructure proved extension of the wavelength regime to 3.5 μm. The Sn content in the shell was 18%, and the compressive strain was –1.3%. The speed of vertical incidence GeSn photodetectors [49] with small areas turned out to be similar (>40 GHz) to Ge photodiodes despite the higher dark currents. High-speed operation has to be confirmed for photodiodes with higher Sn content (>4%) or high tensile strain (>0.25%).

Si-based photonics benefits strongly from the mature technology and precision of fine structure lithography. This allows rapid progress in lateral incidence waveguide photodetectors because of fabrication of small-area photodetectors with high responsivity and high speed. Lateral waveguide photodetectors decouple [7] the influence of layer thickness on responsivity and speed in contrast to vertical photodetectors, in which the responsivity increases with thickness at the cost of speed (Eq. 9.32). In lateral photodetectors, the length of the detector determines the responsivity whereas the thickness and the capacitive load (Fig. 9.23) determine the speed. Precise lithography and sophisticated contact geometries are essential to reduce the parasitic RC limitation of the speed.

Advanced CMOS concepts foresee heterostructure channel materials on Si with a focus on similar material combinations rather than on Si-based photonics, for example, Ge on Si, III/V on Si, and GeSn on Si. To tackle the challenges with such heterostructures, many instances of cooperation between industries and academia emerged and existing foundry services adopted some of these materials in their product portfolios, with astonishing performance. Some of them specialize [50] in passive and active photonic devices for waveguiding in Si and SiN and for detecting in Ge on Si.

Acknowledgments

We thank Michael Oehme for many fruitful discussions.

References

1. E. Kasper (2010). Prospects and challenges of silicon/germanium on-chip optoelectronics, *Front. Optoelectron. China*, **3**, 143–152.
2. C. Penn, T. Fromherz and G. Bauer (2000). Energy gaps and band structure of SiGe and their temperature dependence, EMIS Data Review, Vol. 24 (INSPEC, IEE, England), pp. 125–134.
3. J. Humlicek (2000). Optical functions of the relaxed SiGe alloy, EMIS Data review, Vol. 24 (INSPEC, IEE, England), pp. 249–259.
4. S. M. Sze (1981). *Physics of Semiconductor Devices*, 2nd ed. (John Wiley).
5. S. M. Sze and K. K. Ng (2007). *Physics of Semiconductor Devices*, 3rd ed. (Wiley-Interscience).
6. C. H. Lin and C. W. Liu (2010). Metal-insulator-semiconductor photodetectors, *Sensors*, **10**, 8797–8826
7. J. Michel, J. Liu and L. C. Kimerling (2010). High performance Ge-on-Si photodetectors, *Nat. Photonics*, **4**, 527–534.
8. D. Bougeard, K. Brunner and G. Abstreiter (2003). Intraband photoresponse of SiGe quantum dot/quantum well multilayers, *Physica E*, **16**, 609–613.

9. R. P. G. Karunasiri, J. S. Park and K. L. Wang (1992). Normal incidence infrared detector using intervalence-subband transitions in SiGe/Si quantum wells, *Appl. Phys. Lett.*, **91**, 2234–2236.
10. K. L. Wang, D. Cha, J. Liu and C. Chen (2007). Ge/Si self-assembled quantum dots and their optoelectronic device applications, *Proc. IEEE*, **95**, 1866–1883.
11. M. A. Gadir, P. Harrison and R. A. Soref (2001). Arguments for p-type quantum-well SiGe/Si photodetectors for the far and very-far (terahertz)-infrared, *Superlatt. Microstruct.*, **30**, 135–143.
12. W. S. Ho, C. H. Lin, T. H. Cheng, W. W. Hsu, Y. Y. Chen, P. S. Kuo and C. W. Liu (2009). Narrow-band metal-oxide-semiconductor photodetector, *Appl. Phys. Lett.*, **94**, 061114-1–061114-3.
13. M. Jutzi, M. Berroth, G. Wöhl, M. Oehme and E. Kasper (2005). Ge-on-Si vertical incidence photodiodes with 39-GHz bandwidth, *IEEE Photonics Technol. Lett.*, **17**, 1510–1512.
14. M. Oehme, J. Werner, E. Kasper, M. Jutzi and M. Berroth (2006). High bandwidth Ge p-i-n photodetector integrated on Si, *Appl. Phys. Lett.*, **89**, 071117.
15. E. Kasper and W. Zhang (2015). Device operation as crystal quality probe, in *Silicon, Germanium and their Alloys: Growth, Defects, Impurities and Nanocrystals*, G. Kissinger and S. Pizzini, eds. (Taylor and Francis, Boca Raton), pp. 341–364.
16. M. Oehme, M. Kaschel, J. Werner, O. Kirfel, M. Schmid, B. Bahouchi, E. Kasper and J. Schulze (2010). Germanium on silicon photodetectors with broad spectral range, J. *Electrochem. Soc.*, **157**, H144–H148.
17. G. H. Rieke (1994). *Detection of Light: From the Ultraviolett to the Submillimeter* (Cambridge Univ. Press).
18. C. H. Lin, C. Y. Yu, C. Y. Peng, W. S. Ho and C. W. Liu (2007). Broadband SiGe/Si quantum dot infrared photodetectors, *J. Appl. Phys.*, **101**, 033117-1–033117-4.
19. M. Oehme, J. Werner, O. Kirfel and E. Kasper (2008). MBE growth of SiGe with high Ge content for optical applications, *Appl. Surf. Sci.*, **254**, 6238–6241.
20. M. Kaschel, M. Oehme, O. Kirfel and E. Kasper (2009). Spectral responsivity of fast Ge photodetectors on SOI, *Solid-State Electron.*, **53**, 909–911.
21. M. Oehme, J. Werner, E. Kasper, S. Klinger and M. Berroth (2007). Photocurrent analysis of a fast Ge p-i-n detector on Si, *Appl. Phys. Lett.*, **91**, 051108.

22. M. Schmid, M. Kaschel, M. Gollhofer, M. Oehme, J. Werner, E. Kasper and J. Schulze (2012). Franz-Keldysh effect of germanium-on-silicon p-i-n diodes within a wide temperature range, *Thin Solid Films*, **525**, 110–114.
23. A. Splett, T. Zinke, K. Petermann, E. Kasper, H. Kibbel, H. J. Herzog and H. Presting (1994). Integration of waveguide and photodetectors in SiGe for 1.3 µm operation, *IEEE Photonics Technol. Lett.*, **6**, 59–61.
24. Y. Kang, et al. (2009). Monolithic germanium/silicon avalanche photodiodes with 340 GHz gain-bandwidth product, *Nat. Photonics*, **3**, 59–63.
25. X. Wang, et al. (2009). 80 GHz bandwidth-gain-product Ge/Si avalanche photodetector by selective Ge growth, *OSA Techn. Dig. Optical Fiber Conference*, paper OMR3.
26. N. Duan, T.-Y. Liow, A. E.-J. Lim, L. Ding and G. Q. Lo (2012). 310 GHz gain-bandwidth product Ge/Si avalanche photodetector for 1550 nm light detection, *Opt. Express*, **20**, 11031.
27. H. Kressel (1982). *Semiconductor Devices for Optical Communication* (Springer-Verlag).
28. B. C. Hsu, C. H. Lin, P. S. Kuo, S. T. Chang, P. S. Chen, C. W. Liu, J. H. Lu and C. H. Kuan (2004). Novel MIS Ge-Si quantum-dot infrared photodetectors, *IEEE Electron Device Lett.*, **25**, 544–546.
29. J. L. Liu, W. G. Wu, A. Balandin, G. L. Jin and K. L. Wang (1992). Intersubband absorption in boron-doped multiple Ge quantum dots, *Appl. Phys. Lett.*, **74**, 185–187.
30. P. S. Kuo, C. H. Lin, C. Y. Peng, Y. C. Fu and C. W. Liu (2007). Transport mechanism of SiGe dot MOS tunneling diodes, *IEEE Electron Device Lett.*, **28**, 596–598.
31. M. H. Liao, C. H. Lee, T. A. Hung and C. W. Liu (2007). The intermixing and strain effects on electroluminescence of SiGe dots, *J. Appl. Phys.*, **102**, 053520-1–353520-5.
32. C. H. Lin and C. W. Liu (2010). Metal-oxide-semiconductor SiGe/Si quantum dot infrared photodetectors with delta doping in different positions, *Thin Solid Films*, **518**, 237–240.
33. S. Klinger, M. Berroth, M. Kaschel, M. Oehme and E. Kasper (2009). Ge on Si p-i-n photodiodes with a 3-dB bandwidth of 49GHz, *IEEE Photonics Technol. Lett.*, **21**, 920–922.
34. O. I. Dosunmu, D. D. Cannon, M. K. Emsley, L. C. Kimerling and M. S. Unlu (2005). High-speed resonant cavity enhance Ge photodetectors on reflecting Si substrates for 1550-nm operation, *IEEE Photonics Technol. Lett.*, **17**, 175–177.

35. M. Rouvière, L. Vivien, X. Le Roux, J. Mangeney, P. Crozat, C. Hoarau, E. Cassan, D. Pascal, S. Laval, J. M. Fédéli, J. F. Damlencourt, J. M. Hartmann and S. Kolev (2005). Ultrahigh speed germanium-on-silicon-on-insulator photodetectors for 1.31 and 1.55 μm operation, *Appl. Phys. Lett.*, **87**, 231109.

36. G. Masini, G. Capellini, J. Witzens and C. Gunn (2008). A 1550 nm, 10 Gbps monolithic optical receiver in 130 nm CMOS with integrated Ge waveguide photodetector, *Proc. of the 5th IEEE International Conference on Group IV Photonics*, 28–30.

37. L. Vivien, D. Marris-Morini, J. Mangeney, P. Crozat, E. Cassan, S. Laval, J. M. Fédéli, J. F. Damlencourt and Y. Lecunff (2008). 42 GHz waveguide germanium-on-silicon vertical PIN photodetector, *Proc. of the 5th IEEE International Conference on Group IV Photonics*, 185–187.

38. D. Suh, S. Kim, J. Joo, G. Kim and I. G. Kim (2008). 35 GHz Ge p-i-n photodetectors implemented using RPCVD, *Proc. of the 5th IEEE International Conference on Group IV Photonics*, 191–193.

39. G. Dehlinger, S. J. Koester, J. D. Schaub, J. O. Chu, Q. C. Ouyang and A. Grill (2004). High-speed germanium-on-SOI lateral PIN photodiodes, *IEEE Photonics Technol. Lett.*, **16**, 2547–2549.

40. J. Yu, E. Kasper and M. Oehme (2006). 1.55-um resonant cavity enhanced photodiode based on MBE grown Ge quantum dots, *Thin Solid Films*, **508**, 396–398.

41. M. Steglich, et al. (2015). Ge-on-Si photodiode with black silicon boosted responsivity, *Appl. Phys. Lett.*, **107**, 051103.

42. K. Sun, et al. (2018). Low dark current III–V on silicon photodiodes by heteroepitaxy, *Opt. Express*, **26**, 13605.

43. M. Piels and J. E. Bowers (2012). Si/Ge uni-traveling carrier photodetector, *Opt. Express*, **20**, 7488.

44. E. Kasper (2016). Group IV heteroepitaxy on silicon for photonics, *J. Mater. Res.*, **31**, 3639–3648.

45. H. Lin, Z. Luo, T. Gu, L. C. Kimerling, K. Wada, A. Agarwal and J. Hu (2017). Mid-infrared integrated photonics on silicon: a perspective, *Nanophotonics*, **7**, 393–420.

46. D. J. Lockwood, X. Wu, J.-M. Baribeau, S. A. Mala, X. Wang and L. Tsybeskov (2016). Si/SiGe heterointerfaces in one-, two-, and three-dimensional nanostructures: their effect on SiGe light emission, *ECS Trans.*, **75**, 77–96.

47. X. Wang and J. Liu (2018). Emerging technologies in Si active photonics, *J. Semicond.*, **39**, 061001-1–061001-29.

48. S. Assali, et al. (2017). Growth and optical properties of direct band gap Ge/Ge0.87Sn0.13 core/shell nanowire arrays, *Nano Lett.*, **17**, 1538–1544.

49. M. Oehme, K. Kostecki, K. Ye, et al. (2014). GeSn-on-Si normal incidence photodetectors with bandwidths more than 40 GHz, *Opt. Express*, **22**, 839.

50. http://www.aimphotonics.com/pdk/